APPLIED SCIENCES AND ENGINEERING

Intrinsically stretchable electronics with ultrahigh deformability to monitor dynamically moving organs

Shaolei Wang[1,2], Yuanyuan Nie[1,3], Hangyu Zhu[1,2], Yurui Xu[1,3], Shitai Cao[1,2], Jiaxue Zhang[1,2], Yanyan Li[1,2], Jianhui Wang[1,2], Xinghai Ning[1,3]*, Desheng Kong[1,2]*

Intrinsically stretchable electronics represent an attractive platform for next-generation implantable devices by reducing the mechanical mismatch and the immune responses with biological tissues. Despite extensive efforts, soft implantable electronic devices often exhibit an obvious trade-off between electronic performances and mechanical deformability because of limitations of commonly used compliant electronic materials. Here, we introduce a scalable approach to create intrinsically stretchable and implantable electronic devices featuring the deployment of liquid metal components for ultrahigh stretchability up to 400% tensile strain and excellent durability against repetitive deformations. The device architecture further shows long-term stability under physiological conditions, conformal attachments to internal organs, and low interfacial impedance. Successful electrophysiological mapping on rapidly beating hearts demonstrates the potential of intrinsically stretchable electronics for widespread applications in health monitoring, disease diagnosis, and medical therapies.

INTRODUCTION

Implantable electronics provide personalized platforms for health monitoring, disease diagnosis, and medical therapies by integrating sensing, stimulation, and drug delivery capabilities (*1*–*3*). Despite excellent electronic performances, conventional rigid probes tend to induce long-term inflammatory responses as a result of the large mechanical mismatch with the soft, curvilinear, and dynamic biological tissues (*4*–*7*). To overcome this limitation, stretchable electronics have emerged as a promising technology that features compliant mechanical properties to withstand bending, twisting, and expanding (*8*–*11*). The excellent mechanical deformability is the enabler of conformable and intimate interfaces with skins (*12*–*14*), internal organs (*15*–*19*), and stem cell–derived tissues (*20*, *21*). The seamless integration of functional electronics with biological systems provides an enticing opportunity for the stable collection of rich physiological information and the facile implementation of electrical/chemical simulations.

Currently, several design strategies are available to construct stretchable electronic devices and systems. Strain engineering represents a straightforward approach to convert various thin-film electronic devices into highly extensible structures (*22*, *23*). The open-mesh design in particular has demonstrated excellent deformability on the system level for the intimate interaction with living tissues (*20*) and the facile implantation through syringe injections (*15*, *16*). The inherent high rigidity of conventional electronic materials, however, may still induce notable mechanical constraints on soft biological systems (*24*). An alternative approach makes use of all compliant material components to construct intrinsically stretchable electronic devices (*13*, *17*, *25*), which naturally exhibit skin-like mechanical properties without complicated structural designs. The recent studies have shown the substantial suppression of adverse reactions in these systems because of the improved mechanical compatibility with soft tissues during long-term implantable applications (*21*, *26*, *27*).

Intrinsically stretchable conductors represent a class of key building materials to determine the structural designs and the electronic performances of soft implantable devices. Stretchable nanocomposites are formed by embedding various conductive nanostructures into soft elastomers including carbon nanotubes (*28*, *29*), metal nanowires (*30*, *31*), and metal flakes (*32*). Despite decent conductivity and deformability, the degradations in electromechanical properties of these nanocomposites at fine feature dimensions are unfortunately incompatible with high-density integration (*33*, *34*). Electrically conductive hydrogels and polymers are mechanically compliant and well suited for implantable devices (*35*, *36*). The low electronic conductivity often requires the combination with metal structures and thereby limits the stretchability of corresponding devices (*17*). A eutectic gallium indium (EGaIn) alloy, commonly termed as liquid metal, stands out as a competitive candidate material with excellent electronic conductivity (3.4×10^4 S/cm), low melting point (15.5°C), and liquid-state deformability (*37*, *38*). The negligible toxicity is the enabler for various biomedical applications of liquid metal including drug delivery, cancer therapy, skin-attachable sensors, and electronic blood vessels (*39*, *40*). The flowable characteristics, on the other hand, give rise to insufficient structural stability as the direct interface with dynamically moving tissues and organs. In addition, liquid metals suffer from chemical corrosion under physiological conditions, thereby inhibiting the stable and reliable operation for long-term in vivo applications (*41*, *42*). These practical issues represent the major barriers for the deployment of liquid metal conductors in stretchable and implantable electronics.

In this study, we reported a scalable fabrication of intrinsically stretchable and implantable electronic device featuring low interfacial impedance, ultrahigh stretchability up to 400% tensile strain, excellent durability against repetitive deformations, and long-term stability under physiological conditions. The entire device is completely made of highly compliant electronic materials, including liquid metal interconnects, conductive nanocomposite electrodes, and

[1]College of Engineering and Applied Sciences and Jiangsu Key Laboratory of Artificial Functional Materials, Nanjing University, Nanjing 210046, China. [2]State Key Laboratory of Analytical Chemistry for Life Science, Nanjing University, Nanjing 210046, China. [3]National Laboratory of Solid State Microstructure, Collaborative Innovation Center of Advanced Microstructures, and Chemistry and Biomedicine Innovation Center, Nanjing University, Nanjing 210093, China.
*Corresponding author. Email: dskong@nju.edu.cn (D.K.); xning@nju.edu.cn (X.N.)

microcracked conductive polymer bioelectronic interface. Liquid metal interconnect exhibiting metal-level conductivity of 3.8×10^4 S/cm and liquid-state deformability is the enabler of exceptional stretchability and low signal losses in the device. Stretchable nanocomposite modified by conductive polymer provides a mechanically compatible and electronically stable interface to interact with biological tissues. A soft and stretchable electronic patch is constructed to achieve conformal attachments on rapidly beating hearts and continuous epicardial electrophysiological recording/mapping for over 5000 expansion-contraction cycles. The successful capture of anomalous epicardial electrograms during cardiac arrhythmia demonstrates the potential application of the stretchable electronic patch for the diagnosis of cardiovascular diseases. The design and fabrication demonstrated here offer a general strategy to create robust electronics in deformable form factors for implantable sensing and stimulations.

RESULTS

Design of intrinsically stretchable and implantable electronics

As schematically illustrated in Fig. 1A, an intrinsically stretchable electronic device in the form of a 16-channel sensing patch is completely made of compliant mechanical components, including styrene-ethylene-butylene-styrene (SEBS) elastomer for the substrate/encapsulation, liquid metal for interconnects, carbon nanotube nanocomposite for electrodes, and microcracked conductive polymer as bioelectronic interfaces. In Fig. 1B, an as-prepared device is connected to a flexible polyimide connector as the interface with external recording hardware. The soft and stretchy electronic patch is highly deformable and sufficiently robust to endure various mechanical manipulations including twisting, bending, and stretching, as demonstrated in Fig. 1C. The extreme flexibility associated with the low modulus and thin layout is the enabler for conformal contacts with rough and irregular surfaces as exemplified by the case of a walnut (see Fig. 1D). The compliant mechanical characteristics are essential for the implantable applications of stretchable electronic patch to achieve reliable electromechanical coupling with three-dimensional and constantly moving organs.

Stretchable conductors

As regard the building materials, the liquid metal represents an ideal candidate for stretchable conductors. Bulk liquid metal is passivated by native oxides under ambient conditions and readily cleaned by a short treatment in dilute HCl solution. As shown in Fig. 2A, a nonoxidized liquid metal droplet naturally spreads and adheres to thermally evaporated Cu film with a low contact angle of 30°, which is promoted by the formation of intermetallic compounds through interfacial alloying reaction (*43*, *44*). In contrast, nonoxidized liquid metal exhibits a high contact angle of 130° with the pristine SEBS elastomer, suggesting the lack of affinity. A layer of liquid metal is thereby selectively coated onto patterned Cu film on SEBS substrate, by simply rolling bulk liquid metal over the entire substrate submerged in a dilute HCl bath (see Fig. 2B). The process harnesses the large contrast in wettability to enable scalable fabrication of high-fidelity liquid metal features. An array of line-shaped liquid metal patterns is further created to determine the feature resolution as ~50 μm (see Fig. 2C), which is largely limited by the original Cu templates based on the laser ablation technique. The as-prepared

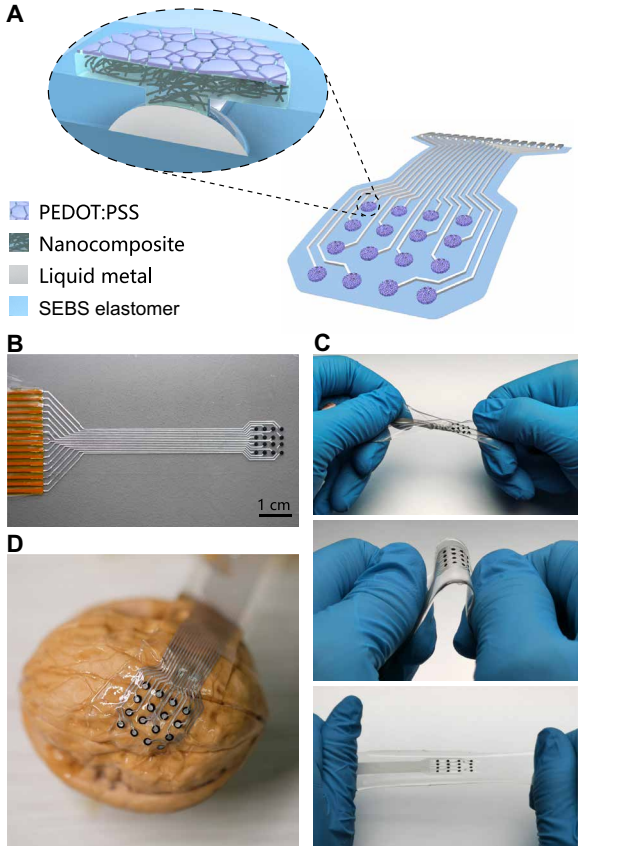

Fig. 1. Intrinsically stretchable electronics in the form of a sensing patch. (**A**) Schematic illustration of the device architecture involving elastomeric encapsulation, liquid metal interconnects, nanocomposite electrodes, and microcracked conductive polymer interface. (**B**) Optical image of an as-prepared electronic patch connected to a flexible polyimide connector. (**C**) Mechanical manipulations of a stretchable patch by twisting (top), bending (middle), and stretching (bottom). (**D**) Conformal attachment of a stretchable device onto a walnut with a rough and curved surface.

liquid metal feature is electrically conductive with a low sheet resistance of 15 milliohms for a typical linewidth of 200 μm. The corresponding electrical conductivity is determined as 3.8×10^4 S/cm based on the cross-sectional area acquired by a confocal scanning laser microscope (see fig. S1). The value is even higher than bulk liquid metal because of the formation of highly conductive intermetallic compounds of $CuGa_2$ and CuGa (*45*). The high conductivity of a stretchable conductor represents a key requirement for the effective suppression of low-frequency losses during long-term recording in physiological conditions (*46*). The native oxides formed on the liquid metal features function as solid shells to retain structural integrity. The subsequent spin casting SEBS dissolved in a slow swelling solvent allows facile encapsulation without noticeable distortions of the liquid metal features (see fig. S2). The stretchability of the liquid metal conductive channel confined in the elastomer is evaluated by measuring their electrical properties in response to uniaxial tensile deformation, as shown in Fig. 2D. The liquid metal conductor is highly deformable to reach tensile strain above 800%. The resistance increases to 3 times at 100% strain, 12 times at 400% strain, and ~30 times at 800% strain, respectively. The giant stretchability is associated with the liquid-state characteristics to accommodate enormous deformations up to the fracture strain of the elastomeric

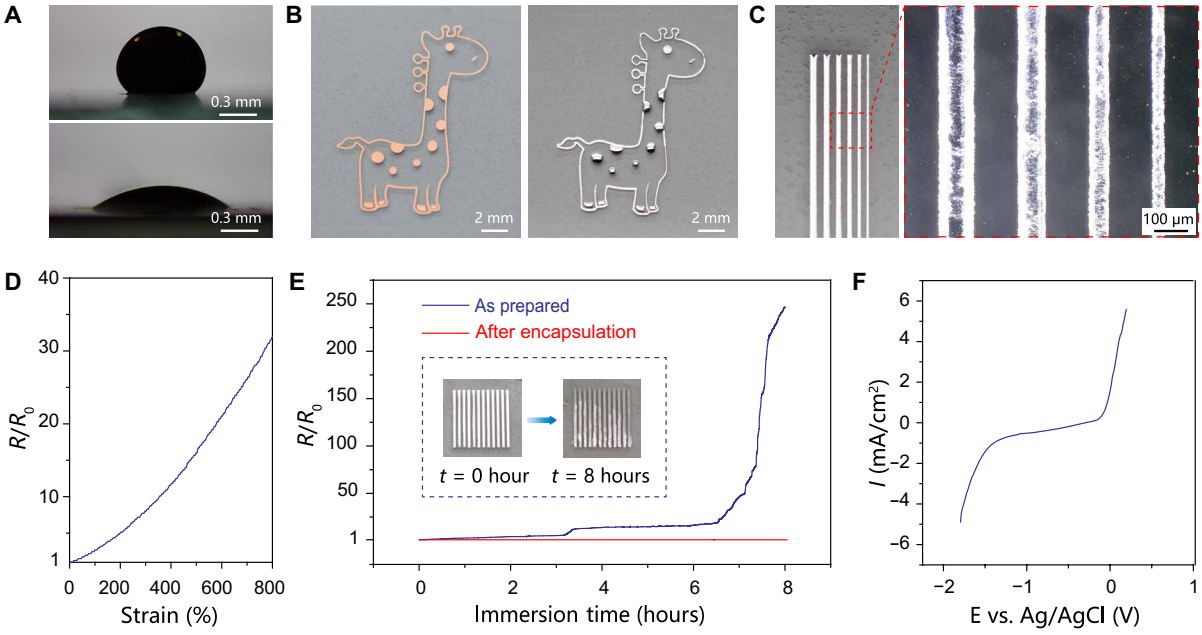

Fig. 2. Patterned liquid metal features. (**A**) Contact angle images of a nonoxidized liquid metal droplet on SEBS elastomer (top) and thermally evaporated Cu film (bottom). (**B**) Optical images of a giraffe-shaped Cu pattern before (left) and after (right) selective coating with a layer of liquid metal, which exhibits obvious color changes from reddish-brown to metallic gray. (**C**) Optical microscopy images of an array of line-shaped features to show the patterning resolution. (**D**) Normalized resistance as a function of uniaxial tensile strain. (**E**) Evolution of the normalized resistance of liquid metal features immersed in PBS solution. Inset: Images showing the visual signatures of chemical corrosion. (**F**) Linear sweep voltammogram of liquid metal in PBS solution to reveal the electrochemical stability window.

matrix. As illustrated in fig. S6, the liquid metal conductor further exhibits negligible changes in the resistance during 1000 stretch-relaxation cycles to 300% strain, which demonstrates the exceptional electromechanical durability for practical applications.

The chemical stability of liquid metal, on the other hand, is less than satisfactory under physiological conditions. Liquid metal features show notable visual signatures of chemical corrosion after immersion in phosphate-buffered saline (PBS) solution for several hours, as shown in the inset of Fig. 2E. The corresponding resistance shows a large increase by over two orders of magnitude within 8 hours (Fig. 2E). In Fig. 2F, the linear sweep voltammogram reveals the electrochemical stability window of liquid metal in PBS solution. The corrosion potential at −0.30 V versus Ag/AgCl reference electrode is consistent with the rapid degradation behaviors (see fig. S3). The process may also release high-concentration gallium and indium ions to induce significant cytotoxicity (*41*). In comparison, the resistance of liquid metal features shows negligible changes after coating with a 25-μm-thick SEBS layer, as shown in Fig. 2E. The retention of fairly stable electrical properties is further verified during one-week storage in PBS solution (see fig. S4). The thin elastomer represents an indispensable encapsulation to ensure the long-term stability of liquid metal features toward implantable applications.

An alternative stretchable conductor compatible with the physiological environment is consequently required for the preparation of functional electrodes to interact with biological systems. Stretchable nanocomposites represent an attractive platform to design conductors with tailored properties. Here, multiwall carbon nanotubes (MWCNTs) are selected as the conductive fillers because of their high electrical conductivity and excellent electrochemical stability (*2*, *29*). A viscous ink is formulated by dispersing MWCNTs into SEBS solution that allows facile and scalable deposition of patterned conductive nanocomposite by stencil printing (see Fig. 3A). An array of line-shaped nanocomposites is further created to reveal the feature resolution as ~100 μm (see Fig. 3A). The printed pattern of 50-μm thickness exhibits a low sheet resistance of ~190 ohms/sq. In the nanocomposite, the three-dimensional percolation network of high–aspect ratio MWCNTs is the enabler of the decent electrical conductivity of ~1.1 S/cm. The electrical properties under uniaxial tensile deformations are shown in Fig. 3B. The normalized resistance is 3 at 50% strain, 12 at 100% strain, and 35 at 150% strain, respectively. The decent stretchability is ascribed to the formation of a structurally continuous and intrinsically deformable conductive network in the SEBS elastomer. The nanocomposite retains intact morphology without obvious cracks at a large tensile strain of 150%, as revealed by scanning electron microscopy (SEM) images in fig. S5. In addition, the stable electrical properties during repetitive tensile deformations are attractive for practical implementations (see fig. S7). In Fig. 3C, the linear sweep voltammogram shows an extremely wide electrochemical stability window of the conductive nanocomposite from −1.25 to 1.30 V, which ensures reliable operations under physiological conditions. In addition, the incorporation of MWCNTs also boosts the mechanical properties of the nanocomposites (fig. S8), which is attributed to the large surface area of MWCNT in contact with the elastomeric matrix for the uniform transfer of applied stress (*47*).

Fabrication and characterizations of the electronic patch

The stretchable bioelectronic patch is constructed by heterogeneous integration of all compliant materials into a thin layout in a layer-by-layer process flow, as schematically illustrated in Fig. 4A. Briefly, liquid metal features are created on SEBS substrate by the solution-based patterning process and then encapsulated by spin casting an

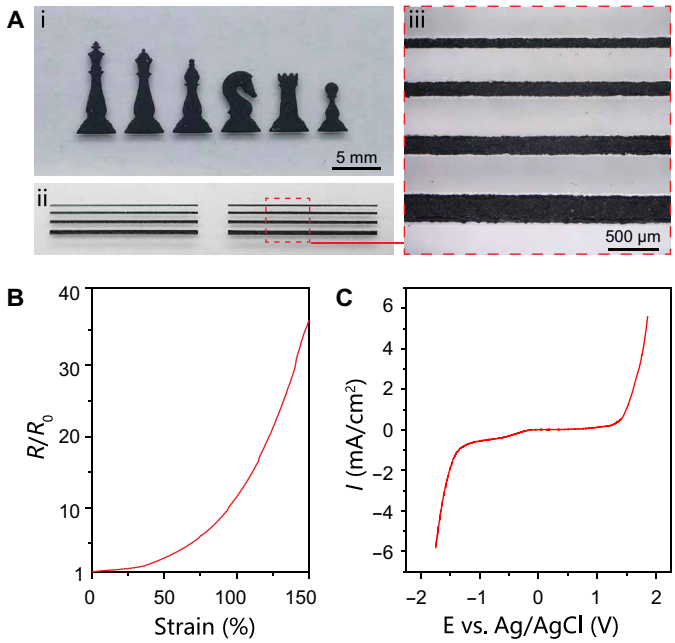

Fig. 3. Printable conductive nanocomposite. (**A**) Stencil-printed nanocomposite feature in the shape of chess pieces and line array to reveal the patterning quality and resolution. (**B**) Normalized resistance as a function of uniaxial tensile strain. (**C**) Linear sweep voltammogram of the nanocomposite in PBS solution to show the electrochemical stability window.

additional SEBS layer. Selective laser ablation on the liquid metal contact pad ruptures the elastomeric encapsulation layer and thereby generates vertical interconnect accesses (VIAs) of ~200 μm in diameter (see fig. S9). Conductive nanocomposite electrodes are subsequently stencil printed over the VIAs to establish electrical connections with the embedded liquid metal interconnects. The total thickness of this patch is about 50 μm. The scalable approach allows facile fabrication of stretchable and implantable electronic patches of different sizes, as illustrated in fig. S10.

Electrochemical impedance spectroscopy is carried out to evaluate the performances of the as-prepared electronic patch. In Fig. 4B, the impedance spectrum reveals a pretty high impedance magnitude of an individual sensing channel, which is likely associated with the limited active surface area of exposed MWCNTs in the nanocomposite. The high impedance represents a major barrier for high-fidelity recording because of significant signal attenuations and distortions. A layer of electrodeposited poly(3,4-ethylenedioxythiophene)–poly(styrenesulfonate) (PEDOT:PSS) is therefore electrochemically deposited onto an individual electrode that substantially reduces the impedance. The notable improvement is ascribed to the high specific capacitance of 61.6 mC cm^{-2} for the PEDOT:PSS layer, as shown in fig. S11. In Fig. 4B, the phase plot of the impedance spectrum further reveals a phase angle close to 0, which suggests the dominance of the resistance component suitable for electrophysiological recording and simulations.

All compliant components render the entire electronic patch soft and stretchy. The pristine elastomer has a large fracture strain of 850% and a low modulus of 1.3 MPa, as shown in fig. S8. The MWCNT nanocomposite retains excellent stretchability with an increased modulus of 5.1 MPa because of the strengthening effects of nanoscale fillers (fig. S8). In Fig. 4C, a series of optical images reveal a representative electronic patch under uniaxial tensile deformation up to 400% strain. The actual strain of an individual electrode linearly increases with the tensile deformation of the entire sensing patch to reach 124% at a high global strain of 400% (Fig. 4D). The modulus contrast gives rise to spatially heterogeneous strain distributions over the electronic patch upon tensile deformations, thereby mitigating the actual strains on sensing electrodes for enhanced stretchability on the system level (*48*). In addition, the similar compositions among all building components ensure robust interfacial interactions to avoid delamination under highly deformed states (*48*). The corresponding impedance at 1 kHz is fairly stable with marginal increase (<20%) under tensile deformations up to 300% strain (Fig. 4E). A noticeable increase by two times is observed at 400% strain that is ascribed to the largely increased series resistance of the nanocomposite electrode.

The low interfacial impedance is essential for the reliable acquisitions of electrophysiological signals (*17*). Although the interconnects and electrodes are based on compliant materials, the as-deposited PEDOT:PSS interface layer is fairly brittle with limited stretchability (*49*, *50*). The strain-insensitive impedance is largely associated with the unique architecture of the sensing electrode. In Fig. 4F, SEM images of the sensing electrode at pristine and stretched states are shown to reveal the crack of the PEDOT:PSS layer into numerous islands. The attachment of brittle films onto an elastomeric substrate is an effective approach to suppress the propagations of large cracks upon tensile deformations, thereby spontaneously generating fine islands to release the tensile stress (*51*, *52*). Despite the apparently broken morphology, the microcracked PEDOT:PSS layer is still fully functional because of the excellent contact with the underlying stretchable conductive nanocomposite (see fig. S12). In Fig. 4E and fig. S13, the electrochemical capacitance and corresponding interfacial impedance of the PEDOT:PSS layer show negligible changes with the formation of the microcracked morphology because of the volumetric charge storage mechanism (*53*, *54*).

A robust construction is essential for the practical applications of the stretchable electronic patch. The electromechanical durability is assessed by tensile fatigue tests on as-prepared electronic patches. Individual sensing channels retain stable impedance amplitude during 10,000 stretch-relaxation cycles to 100% strain (see Fig. 4G and fig. S14). In addition, the chemical stability of the electronic patch is evaluated through long-term storage in PBS solution. The individual sensing channels are well operational with marginally increased impedance under both relaxed and stretched states, as illustrated in fig. S15.

In vivo recording on beating hearts

The implantable epicardial recording process provides valuable information for discovering and monitoring cardiovascular diseases (*17*, *25*, *31*). The biocompatibility of the stretchable electronic patch has been verified by cell viability analyses, as summarized in figs. S16 and S17. The electronic patch is consequently used to acquire epicardial electrograms from beating hearts of bullfrogs. As schematically illustrated in Fig. 5A, the sensing patch is attached to the surface of the ventricle, whereas a Pt needle reference electrode was subcutaneously inserted into the right leg. The intrinsic stretchability of the electronic patch ensures conformal contacts to the heart without sliding and delamination during cardiac expansion and contraction cycles (see Fig. 5B and movie S1). Figure 5C shows

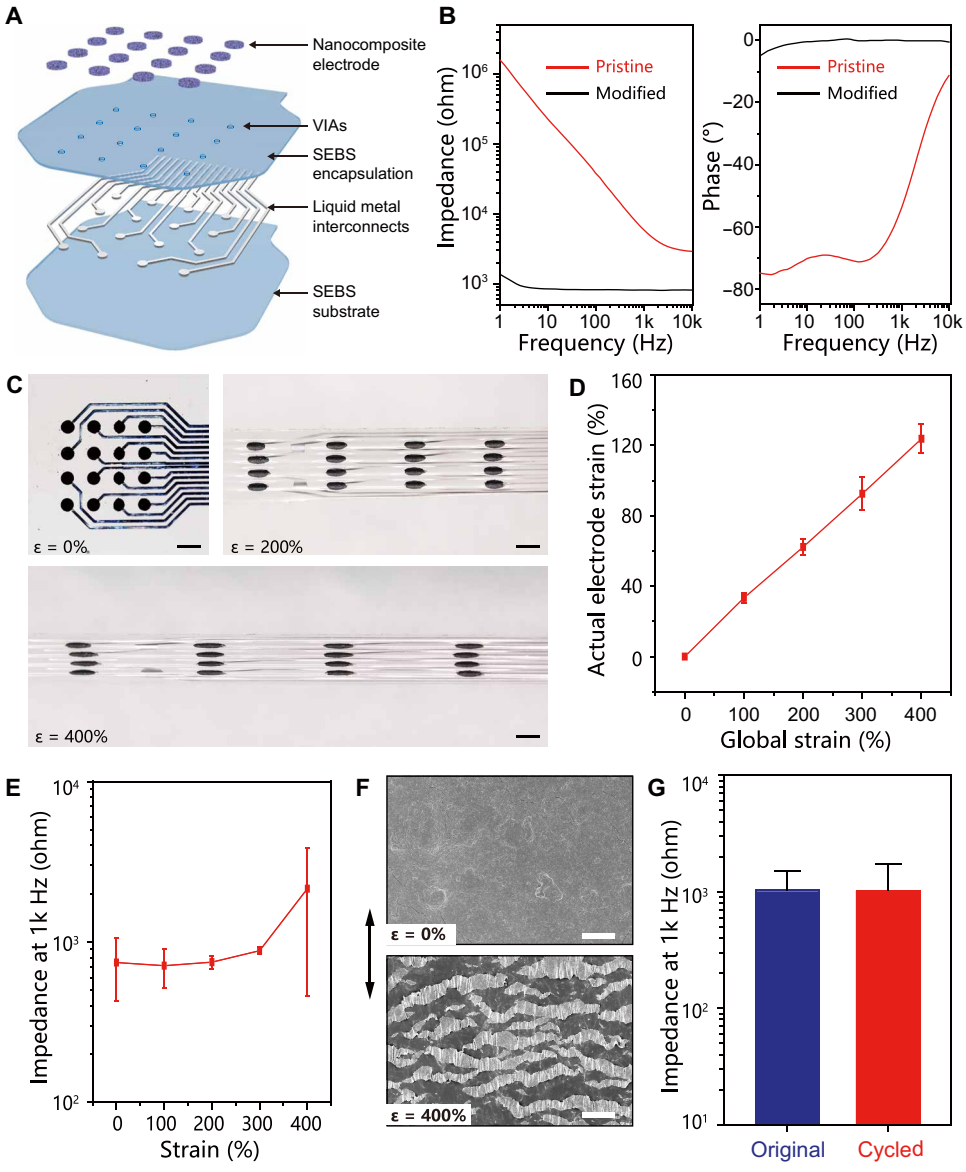

Fig. 4. Integrated stretchable electronic patch. (**A**) Schematic showing the layer-by-layer construction of the electronic patch. (**B**) Impedance and phase angle spectra of an individual sensing channel at the pristine state and after modification with a PEDOT:PSS layer. (**C**) Images of the stretchable electronic patch at different tensile strains. Scale bars, 2 mm. (**D**) Correlation of the local strain of individual sensing electrode with the global strain of the electronic patch. (**E**) Impedance of individual channels on the electronic patch at 1 kHz at various applied strain up to 400%. (**F**) SEM images of the sensing electrode on the pristine (top) and stretched (bottom, 400% strain) patch, in which the arrow indicates the stretching direction. Scale bars, 50 μm. (**G**) Impedance of an individual channel at the original state and after 10,000 stretch-relaxation circles to 100% strain.

representative electrograms acquired from the anterior ventricular surface by the electronic patch. The microcracked PEDOT:PSS interface layer is effective to improve the signal quality by substantially reducing the interfacial electrochemical impedance, as shown in Fig. 5E. Specifically, the signal amplitude is increased from 2.17 ± 0.23 to 6.32 ± 0.41 mV, and the signal-to-noise ratio (SNR) is enhanced from 69.7 ± 7.4 to 263.2 ± 16.9 (Fig. 5D). All 16 sensing channels are fully functional to enable spatially and temporally resolved biopotential mapping (see fig. S18). In Fig. 5F, spatiotemporal epicardial-potential maps capture cardiac activation propagating from the top left to the bottom right of the array during a sinus rhythm. The activation time is determined by using the maximum negative slope (dV/dt) of each electrogram trace to obtain the isochronal map, as shown in Fig. 5G. The isochronal map suggests the propagation speed of the action potential is 1.2 m/s on the heart surface, which is comparable to the typical values of frog muscle tissues (*55*). The average heart rate of ~33 beat/min is consistent with previous reports (*56*). Accordingly, the soft and deformable patch allows direct and intimate attachment on slowly moving organs for the reliable collection of electrophysiological signals.

The dynamic and fast-moving organs present practical challenges for implantable electronics to achieve direct contact mapping. The demanding measurement condition is a relevant clinical application as exemplified by atrial fibrillation accompanied by fast and chaotic

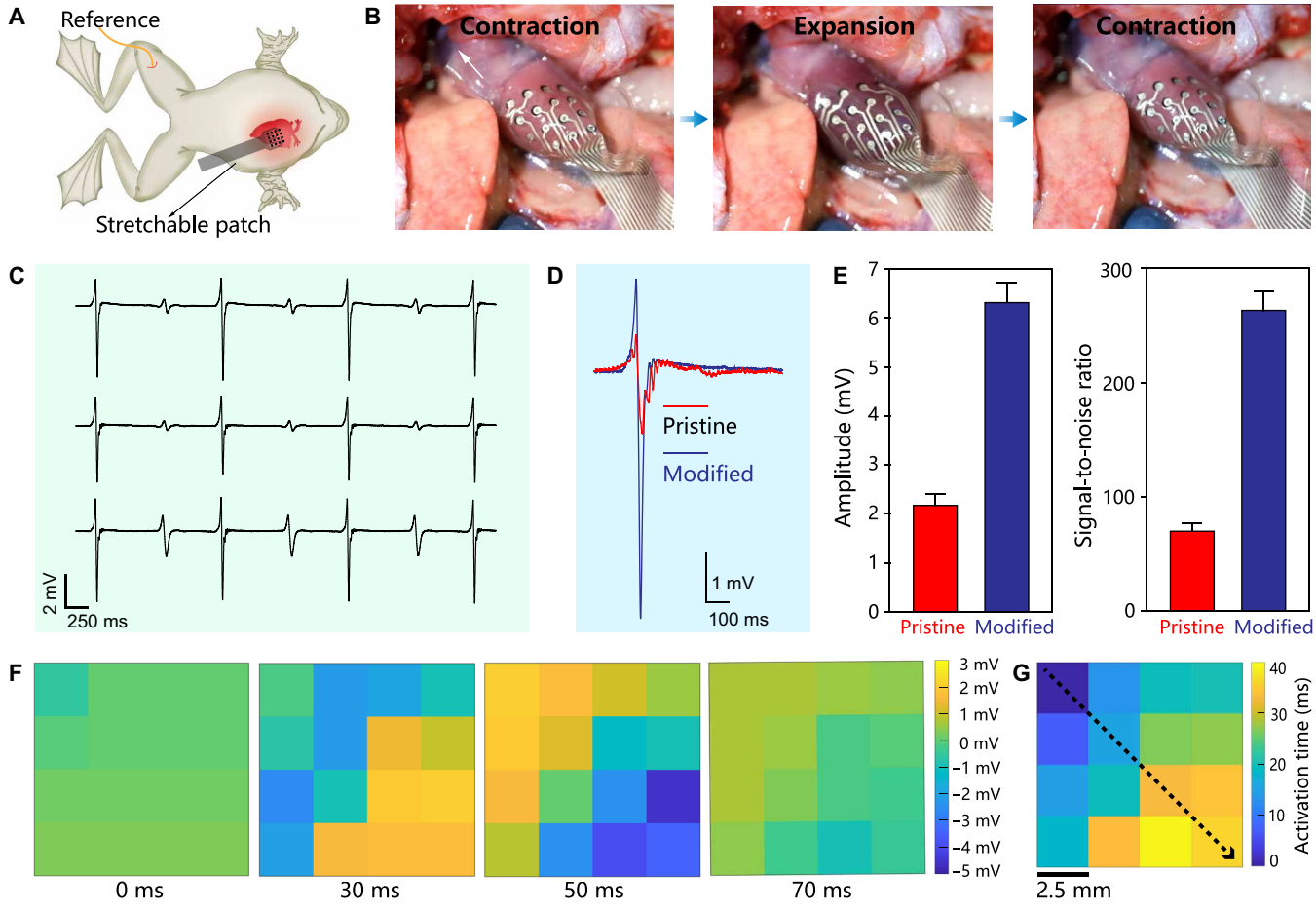

Fig. 5. In vivo epicardial recording on a bullfrog. (**A**) Schematic illustration of the experimental setup for epicardial electrogram acquisition from a living bullfrog. (**B**) Optical images showing the conformal attachment of the electronic patch to the surface of a bullfrog heart under contractions and expansions during one cardiac cycle. (**C**) A series of epicardial electrograms. (**D**) Representative single voltage traces acquired by the sensing electrode before and after modified with PEDOT:PSS layer. (**E**) Statistical analysis of signal amplitude and SNR. (**F**) Spatiotemporal biopotential map from all 16 channels at four sequential time points of a sinus rhythm. (**G**) Activation map of the sinus rhythm captured by the stretchable electronic patch, in which the dotted arrow indicates the progression direction of the electric signals.

ventricular responses. Rabbit hearts are selected as the model systems to evaluate the performance of the stretchable electronics during rapid cardiac cycles. A rabbit was mechanically ventilated and underwent a thoracotomy to expose the heart, followed by the attachment of the electronic patch onto the surface of the right ventricular (Fig. 6A). The epicardial electrograms were successfully acquired in almost all channels (see fig. S19). As compared with the case of the bullfrog, the irregular fluctuations and increased noise level in the electrograms are likely associated with the reduced electromechanical coupling of the electronic patch with the rapidly beating heart of the rabbit. A polydopamine-polyacrylamide hydrogel was consequently synthesized harnessing mussel-inspired chemistry for strong adhesion with wet tissues (*17*), which secures the electronic patch on the beating heart as illustrated in fig. S20. The soft patch consequently achieves conformal and stable contact with the epicardium during cardiac contractions and expansions (see Fig. 6B and movie S2). The representative epicardial electrograms are shown in Fig. 6C. As the hydrogel adhesive effectively suppresses the sliding on the dynamic tissue, the recording quality of the electronic patch is substantially improved in terms of signal amplitude from 1.21 ± 0.30 to 3.76 ± 0.78 mV and the SNR from 40 ± 9 to 137 ± 8 (see Fig. 6, D and E). The heart rate is determined as ~270 bpm and consistent with previous reports (*57*). In Fig. 6F, spatiotemporal epicardial-potential maps are established on the basis of the reliable operations of all sensing channels on the electronic patch, which reveal the horizontal propagation of cardiac activation from the left to the right during a sinus rhythm. In addition, the device supports continuous epicardial recording for 20 min involving over 5000 cardiac contraction-expansion cycles, which demonstrates the exceptional electromechanical durability for long-term operations (see Fig. 6F). All 16 channels are fully functional across the entire recording duration, as shown in fig. S21.

In addition to healthy conditions, a drug-induced cardiac arrhythmia was established in the rabbit model by intravenous administration of $BaCl_2$ solution to impair the ion channels of cardiomyocytes (*58*). According to figs. S22 and S23, abnormal signatures of cardiac arrhythmia are captured by the electronic patch in multiple recording channels in terms of widened QRS complexes for ventricular premature contraction and chaotic fluctuations for fibrillation (*59*). Propranolol therapy was subsequently implemented as medical treatment. The sinus rhythm was largely recovered after intravenous administration despite significant bradycardia with a reduced heart

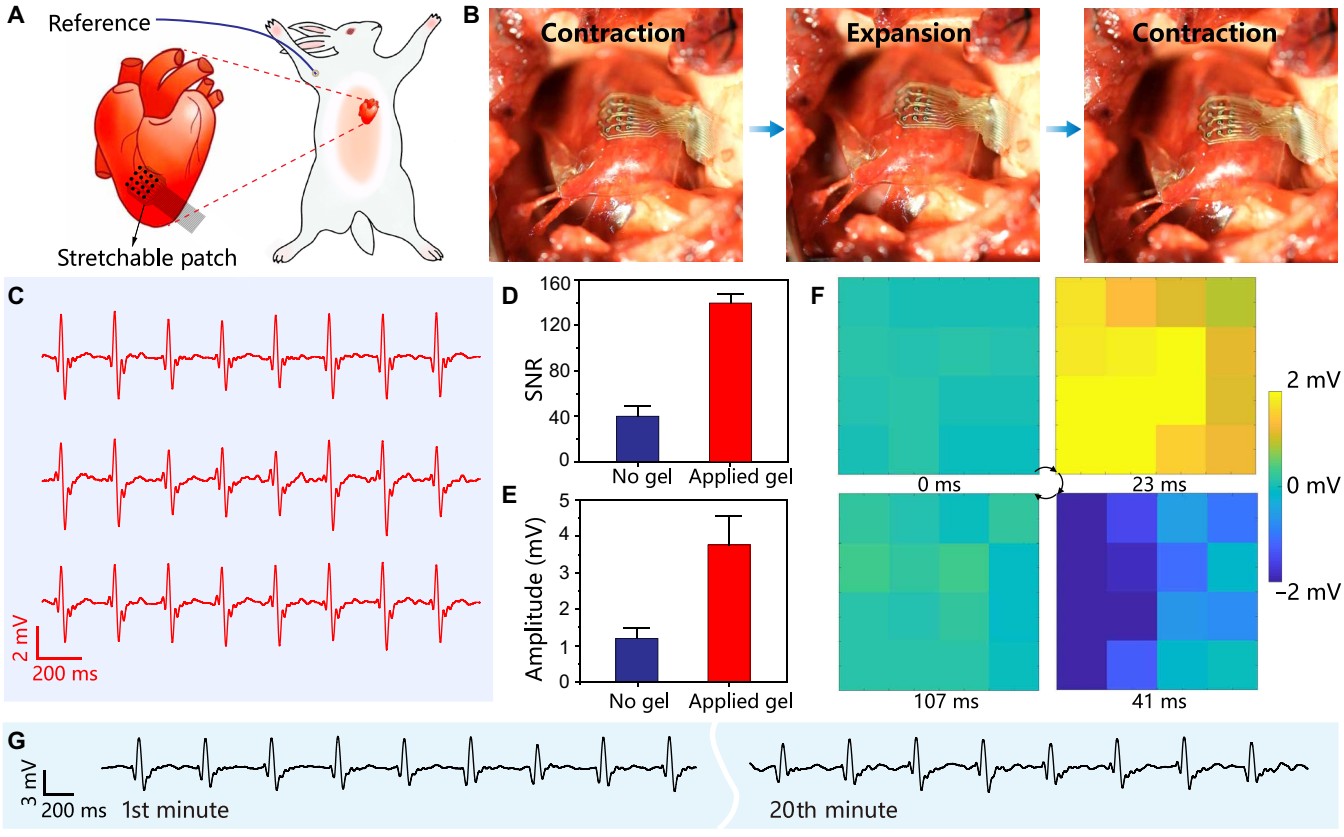

Fig. 6. In vivo epicardial recording on a rabbit. (**A**) Schematic illustration of the experimental setup for epicardial electrogram acquisition from a living rabbit. (**B**) Stretchable electronic patch achieving conformal attachment to the right ventricle by using a hydrogel adhesive. (**C**) A series of representative epicardial electrograms. (**D** and **E**) Statistical analysis of SNR (D) and amplitude (E) before and after applying the hydrogel adhesive. (**F**) Spatiotemporal biopotential map at four time points of a sinus rhythm. (**G**) A representative electrogram acquired during continuous epicardial recording for 20 min.

rate of ~144 bpm as the side effect. Accordingly, the high-quality electrograms acquired by the stretchable electronic patch may provide valuable information for cardiovascular disease diagnosis and treatment.

DISCUSSION

In conclusion, an intrinsically stretchable and implantable electronic device is constructed by the heterogeneous integration of all compliant material components through a facile and scalable fabrication process. The soft and stretchy device allows conformal and intimate interactions with dynamically moving biological tissues with largely reduced mechanical discrepancy. The exceptional deformability and durability are largely associated with the deployment of liquid metal conductors confined in an elastomeric matrix to build interconnects. Stretchable MWCNT nanocomposite prevents the direct contact of liquid metal with biological systems to ensure the long-term stability of the device in the physiological environment. The stretchable electronic patch allows reliable acquisition of multichannel electrograms on living hearts of animals with distinctive heart rates. The spatiotemporal biopotential maps are established to reveal the propagations of the cardiac activations during sinus rhythms. The successful capture of abnormal electrograms associated with cardiovascular symptoms demonstrates the practical relevance for disease diagnosis and treatment. All the key characteristics of the stretchable electronic patch are highly competitive among recent studies as summarized in table S1. The material developments and fabrication techniques reported in this study may open up an enticing avenue for soft implantable electronics.

MATERIALS AND METHODS

Materials

All chemical reagents were commercially available, including polyvinyl alcohol [PVA; M_W (molecular weight) = 67000], acrylamide, bisacrylamide, ammonium persulfate, dopamine hydrochloridep, tetramethylethylenediamine, barium chloride ($BaCl_2$), and PBS (0.01 M, pH 7.4) from Shanghai Aladdin Bio-Chem Technology Co. Ltd.; 3,4-ethylenedioxythiophene (EDOT) and poly(sodium 4-styrenesulfonate) (NaPSS) from Shanghai Macklin Biochemical Co. Ltd.; and 3% (w/w) pelltobarbitalum natricum and 0.1% propranolol from GlpBio Technology. MWCNTs of 20 to 100 μm in length and 10 to 20 nm in diameter (XFQ041) were purchased from Nanjing XFNANO Technology Co. Ltd. SEBS (H1221) was provided by Asahi Kasei Corporation. The liquid metal, EGaIn alloy, was prepared by melting a mixture of gallium and indium in a weight ratio 75.5:24.5 at 80°C for 2 hours inside a glovebox. As regard the formulation of the printable MWCNT/SEBS nanocomposite, 50-mg MWCNTs were ultrasonically dispersed into 10 ml of toluene for 20 min, manually mixed with 1.5 g of SEBS solution [20% (w/w) in

toluene], and then homogenized at 1000 rpm for 20 min in a planetary mixer (JF-RVITV-150, Shenzhen Junfeng Technology Co. Ltd.). The polydopamine-polyacrylamide hydrogel was prepared by dissolving 2 g of acrylamide, 4 mg of bisacrylamide, 100 mg of ammonium persulfate, and 2 mg of dopamine in 10 ml of tris buffer (pH 8.5). After the addition of 90 μl of tetramethylethylenediamine, the solution was immediately drop cast onto an octadecyltrichlorosilane-modified glass wafer and cured at 60°C for 1 hour, thereby yielding a hydrogel film of ~0.5 mm in thickness.

Characterizations

Optical images and videos were acquired by a Fujifilm X-T10 camera. Microstructures were revealed by optical microscopy (Keyence VHX-6000 digital microscope) and SEM (Zeiss Ultra 55 field emission scanning electron microscope). Surface topographical images and thickness measurements were performed using a confocal laser scanning microscope (VK-X1000, Keyence). The mechanical properties were acquired by using a universal testing machine (Shimadzu AGS-X) equipped with a 50-N load cell. All tensile measurements were carried out with rectangular specimens (100 mm × 5 mm) at a speed of 10 mm/min. The adhesive force was measured under the standard 90° peel configuration at a speed of 50 mm/min. A polydopamine-polyacrylamide hydrogel sample was prepared by curing the precursor on a 10-μm-thick polyethylene terephthalate (PET) as the stiff backing layer. A biological tissue sample was prepared by pasting porcine epicardium slice to a 3-mm-thick acrylic plate with a butylcyanoacrylate glue (Beijing Compont Medical Device Co. Ltd.). The resistance was measured based on 4-point probe method with a Keithley 2110 digital multimeter. The tensile strains were applied by using homemade motorized/manual linear stages. The electrochemical characterizations were carried out under a three-electrode configuration by using a CHI660E workstation (ChenHua, China). The electrochemical stability window was measured by linear sweep voltammetry at a scan rate of 1 mV/s in PBS solution. Electrochemical impedance spectroscopy (EIS) was measured in the frequency range from 1 Hz to 100 kHz with a 5-mV amplitude at the open-circuit potential.

Device fabrication

A 20-μm-thick SEBS film was spin casted from its solution in toluene onto a glass wafer modified with a PVA sacrificial layer. A Cr/Cu (10 nm/100 nm) film was thermally evaporated onto the SEBS substrate and then patterned by selective laser ablation into arbitrary pattern in a 1064-nm laser marking system (XM-FB30, Xianming Optoelectronic Equipment Co. Ltd). The pattern design consists of contact pads in a 4 × 4 square array and corresponding interconnects. The Cu pattern is selectively coated with a layer of liquid metal after rolling bulk liquid metal over the substrate submerged in dilute hydrogen chloride solution [4% (w/v)], followed by rinsing in deionized water and drying at 60°C for 10 min. A 25-μm-thick SEBS film was subsequently spin coated, from its solution in hexane, over the substrate to encapsulate the liquid metal pattern. The VIAs to the embedded liquid metal patterns were created by selective laser ablation at the contact pads, in which ablated materials puncture the elastomeric encapsulation. MWCNT/SEBS nanocomposite electrodes were stencil printed onto the VIA locations by using a stainless steel stencil and thoroughly dried in an oven at 60°C for 2 hours. PEDOT:PSS film was subsequently electrodeposited onto an MWCNT/SEBS nanocomposite electrode as an interface layer. The electrodeposition was carried by using an electrochemical CHI660E workstation under a three-electrode configuration with individual MWCNT/SEBS nanocomposite electrode as the working electrode, graphite rod as the counter electrode, and Ag/AgCl as the reference electrode. An aqueous solution of 0.01 M EDOT and 0.1 M PSS was prepared as the electrolyte for cyclic voltammetry electrodeposition at a scan rate of 50 mV/s in the voltage window between −0.5 and 1.2 V for 20 cycles.

Biocompatibility test

In vitro biocompatibility was evaluated on the basis of normal liver cell line L02 and fibroblast cell lines from the American Type Culture Collection. In 96-well plates, the cells (5000 per well) were seeded and cultured at 37°C for 24 hours. The medium was then replaced with fresh medium containing the testing sample. After the incubation period (24, 48, or 72 hours), a 20-μl 3-(4,5-dimethylthialzol-2-yl)-2,5-diphenyltetrazolium bromide solution (5 mg/ml) was added to each well and incubated for 4 hours. The medium in each well was replaced with 150 μl of dimethyl sulfoxide. Absorbance was measured at 570 nm by using a microplate reader (Tecan Group). In addition, the incubated cells were washed with PBS and stained with calcein AM (1 μl, 1 mg/ml) for 30 min, followed by imaging with a fluorescence microscope (Tecan Group).

In vivo animal experiments

All animal protocols were approved by the Animal Care and Use Committee of Nanjing University and conformed to the *Guidelines for the Care and Use of Laboratory Animals* published by the National Institutes of Health. The Number of Animal Use Permit was SYXK(Su)2019-0056. A pithed bullfrog (~500 g, 6 months old, female) was under thoracotomy surgery to expose the anterior surface of the heart. The stretchable electronic patch was laminated onto the surface of the ventricle. A Pt wire of 0.5 mm in diameter was inserted subcutaneously at its leg as the reference electrode. The flexible cable of the patch was connected through a home-built adapter board to an Intan RHD2132 amplifier (Intan Technologies LLC.). All channels were bandpass filtered, preamplified, and then recorded at a sampling rate of 10 kHz. The recorded data were further processed with a home-built MATLAB code. A filter with a bandwidth of 0.1 to 40 Hz was applied for the electrogram data. After applying the filter, the SNR was calculated by the maximum peak of signal and root mean square of the noise region. A rabbit model was used to evaluate the performance of the electronic patch on a rapidly beating heart. A New Zealand white rabbit (~2.5 kg, 3 months old, male) was anesthetized by intravenous injection of 10 ml of 3% (w/w) pelltobarbitalum natricum in PBS solution through auricular vein. The rabbit was placed in a supine position over a heating pad with the hair removed from the chest and the foreleg. The rabbit underwent endotracheal intubation and mechanical ventilation using a pressure ventilator (ALC-V8-L100, Shanghai Alcott Biotech Co. Ltd.). A thoracotomy was performed to expose the heart with the pericardium removed by fine forceps. The electronic patch was laminated on the right ventricle. An additional hydrogel adhesive was attached to the entire exposed heart for enhanced electromechanical coupling. Ag/AgCl gel electrode (2223CN, 3M Company) was attached on the skin of the foreleg as the reference. The data recording and analysis were carried out in a similar procedure. A drug-induced cardiac arrhythmia model was established on the basis of $BaCl_2$ to impair ion channels in cardiomyocytes. $BaCl_2$ solution [0.4 weight % (wt %) in normal saline] was administered

through the auricular vein at a dose of 8 mg/kg within 20 s. Cardiac arrhythmia was observed at ~30 s after injection. The propranolol solution (0.1 wt % in normal saline) was used as the pharmacological treatment by intravenous administration at a dose of 0.25 mg/kg. The epicardial electrograms were monitored by using the electronic patch.

SUPPLEMENTARY MATERIALS

Supplementary material for this article is available at https://science.org/doi/10.1126/sciadv.abl5511

REFERENCES AND NOTES

1. X. Xie, J. C. Doloff, V. Yesilyurt, A. Sadraei, J. J. McGarrigle, M. Omami, O. Veiseh, S. Farah, D. Isa, S. Ghani, I. Joshi, A. Vegas, J. Li, W. Wang, A. Bader, H. H. Tam, J. Tao, H.-j. Chen, B. Yang, K. A. Williamson, J. Oberholzer, R. Langer, D. G. Anderson, Reduction of measurement noise in a continuous glucose monitor by coating the sensor with a zwitterionic polymer. *Nat. Biomed. Eng.* **2**, 894–906 (2018).
2. L. Wang, S. Xie, Z. Wang, F. Liu, Y. Yang, C. Tang, X. Wu, P. Liu, Y. Li, H. Saiyin, S. Zheng, X. Sun, F. Xu, H. Yu, H. Peng, Functionalized helical fibre bundles of carbon nanotubes as electrochemical sensors for long-term in vivo monitoring of multiple disease biomarkers. *Nat. Biomed. Eng.* **4**, 159–171 (2020).
3. H. Joo, Y. Lee, J. Kim, J.-S. Yoo, S. Yoo, S. Kim, A. K. Arya, S. Kim, S. H. Choi, N. Lu, H. S. Lee, S. Kim, S.-T. Lee, D.-H. Kim, Soft implantable drug delivery device integrated wirelessly with wearable devices to treat fatal seizures. *Sci. Adv.* **7**, eabd4639 (2021).
4. J. W. Salatino, K. A. Ludwig, T. D. Y. Kozai, E. K. Purcell, Glial responses to implanted electrodes in the brain. *Nat. Biomed. Eng.* **1**, 862–877 (2017).
5. J.-W. Jeong, G. Shin, S. I. Park, K. J. Yu, L. Xu, J. A. Rogers, Soft materials in neuroengineering for hard problems in neuroscience. *Neuron* **86**, 175–186 (2015).
6. J. Rivnay, H. Wang, L. Fenno, K. Deisseroth, G. G. Malliaras, Next-generation probes, particles, and proteins for neural interfacing. *Sci. Adv.* **3**, e1601649 (2017).
7. S. P. Lacour, G. Courtine, J. Guck, Materials and technologies for soft implantable neuroprostheses. *Nat. Rev. Mater.* **1**, 16063 (2016).
8. S. Choi, H. Lee, R. Ghaffari, T. Hyeon, D.-H. Kim, Recent advances in flexible and stretchable bio-electronic devices integrated with nanomaterials. *Adv. Mater.* **28**, 4203–4218 (2016).
9. S. Wang, J. Y. Oh, J. Xu, H. Tran, Z. Bao, Skin-inspired electronics: An emerging paradigm. *Acc. Chem. Res.* **51**, 1033–1045 (2018).
10. N. Matsuhisa, X. Chen, Z. Bao, T. Someya, Materials and structural designs of stretchable conductors. *Chem. Soc. Rev.* **48**, 2946–2966 (2019).
11. L. Xu, S. R. Gutbrod, A. P. Bonifas, Y. Su, M. S. Sulkin, N. Lu, H.-J. Chung, K.-I. Jang, Z. Liu, M. Ying, C. Lu, R. C. Webb, J.-S. Kim, J. I. Laughner, H. Cheng, Y. Liu, A. Ameen, J.-W. Jeong, G.-T. Kim, Y. Huang, I. R. Efimov, J. A. Rogers, 3D multifunctional integumentary membranes for spatiotemporal cardiac measurements and stimulation across the entire epicardium. *Nat. Commun.* **5**, 3329 (2014).
12. D.-H. Kim, N. Lu, R. Ma, Y.-S. Kim, R.-H. Kim, S. Wang, J. Wu, S. M. Won, H. Tao, A. Islam, K. J. Yu, T.-i. Kim, R. Chowdhury, M. Ying, L. Xu, M. Li, H.-J. Chung, H. Keum, M. McCormick, P. Liu, Y.-W. Zhang, F. G. Omenetto, Y. Huang, T. Coleman, J. A. Rogers, Epidermal electronics. *Science* **333**, 838–843 (2011).
13. S. Wang, J. Xu, W. Wang, G.-J. N. Wang, R. Rastak, F. Molina-Lopez, J. W. Chung, S. Niu, V. R. Feig, J. Lopez, T. Lei, S.-K. Kwon, Y. Kim, A. M. Foudeh, A. Ehrlich, A. Gasperini, Y. Yun, B. Murmann, J. B. H. Tok, Z. Bao, Skin electronics from scalable fabrication of an intrinsically stretchable transistor array. *Nature* **555**, 83–88 (2018).
14. S. Xu, Y. Zhang, L. Jia, K. E. Mathewson, K.-I. Jang, J. Kim, H. Fu, X. Huang, P. Chava, R. Wang, S. Bhole, L. Wang, Y. J. Na, Y. Guan, M. Flavin, Z. Han, Y. Huang, J. A. Rogers, Soft microfluidic assemblies of sensors, circuits, and radios for the skin. *Science* **344**, 70–74 (2014).
15. J. Liu, T. M. Fu, Z. Cheng, G. Hong, T. Zhou, L. Jin, M. Duvvuri, Z. Jiang, P. Kruskal, C. Xie, Z. Suo, Y. Fang, C. M. Lieber, Syringe-injectable electronics. *Nat. Nanotechnol.* **10**, 629–636 (2015).
16. G. Hong, T.-M. Fu, M. Qiao, R. D. Viveros, X. Yang, T. Zhou, J. M. Lee, H.-G. Park, J. R. Sanes, C. M. Lieber, A method for single-neuron chronic recording from the retina in awake mice. *Science* **360**, 1447–1451 (2018).
17. J. Liu, X. Zhang, Y. Liu, M. Rodrigo, P. D. Loftus, J. Aparicio-Valenzuela, J. Zheng, T. Pong, K. J. Cyr, M. Babakhanian, J. Hasi, J. Li, Y. Jiang, C. J. Kenney, P. J. Wang, A. M. Lee, Z. Bao, Intrinsically stretchable electrode array enabled in vivo electrophysiological mapping of atrial fibrillation at cellular resolution. *Proc. Natl. Acad. Sci. U.S.A.* **117**, 14769–14778 (2020).
18. L. Luan, X. Wei, Z. Zhao, J. J. Siegel, O. Potnis, C. A. Tuppen, S. Lin, S. Kazmi, R. A. Fowler, S. Holloway, A. K. Dunn, R. A. Chitwood, C. Xie, Ultraflexible nanoelectronic probes form reliable, glial scar–free neural integration. *Sci. Adv.* **3**, e1601966 (2017).
19. W. Lee, S. Kobayashi, M. Nagase, Y. Jimbo, I. Saito, Y. Inoue, T. Yambe, M. Sekino, G. G. Malliaras, T. Yokota, M. Tanaka, T. Someya, Nonthrombogenic, stretchable, active multielectrode array for electroanatomical mapping. *Sci. Adv.* **4**, eaau2426 (2018).
20. Q. Li, K. Nan, P. Le Floch, Z. Lin, H. Sheng, T. S. Blum, J. Liu, Cyborg organoids: Implantation of nanoelectronics via organogenesis for tissue-wide electrophysiology. *Nano Lett.* **19**, 5781–5789 (2019).
21. S. Lee, D. Sasaki, D. Kim, M. Mori, T. Yokota, H. Lee, S. Park, K. Fukuda, M. Sekino, K. Matsuura, T. Shimizu, T. Someya, Ultrasoft electronics to monitor dynamically pulsing cardiomyocytes. *Nat. Nanotechnol.* **14**, 156–160 (2019).
22. R. Libanori, R. M. Erb, A. Reiser, H. Le Ferrand, M. J. Süess, R. Spolenak, A. R. Studart, Stretchable heterogeneous composites with extreme mechanical gradients. *Nat. Commun.* **3**, 1265 (2012).
23. D.-H. Kim, J. Xiao, J. Song, Y. Huang, J. A. Rogers, Stretchable, curvilinear electronics based on inorganic materials. *Adv. Mater.* **22**, 2108–2124 (2010).
24. J. Viventi, D.-H. Kim, J. D. Moss, Y.-S. Kim, J. A. Blanco, N. Annetta, A. Hicks, J. Xiao, Y. Huang, D. J. Callans, J. A. Rogers, B. Litt, A conformal, bio-interfaced class of silicon electronics for mapping cardiac electrophysiology. *Sci. Transl. Med.* **2**, 24ra22 (2010).
25. K. Sim, F. Ershad, Y. Zhang, P. Yang, H. Shim, Z. Rao, Y. Lu, A. Thukral, A. Elgalad, Y. Xi, B. Tian, D. A. Taylor, C. Yu, An epicardial bioelectronic patch made from soft rubbery materials and capable of spatiotemporal mapping of electrophysiological activity. *Nat. Electron.* **3**, 775–784 (2020).
26. Y. Liu, J. Li, S. Song, J. Kang, Y. Tsao, S. Chen, V. Mottini, K. McConnell, W. Xu, Y.-Q. Zheng, J. B. H. Tok, P. M. George, Z. Bao, Morphing electronics enable neuromodulation in growing tissue. *Nat. Biotechnol.* **38**, 1031–1036 (2020).
27. S.-H. Sunwoo, S. I. Han, H. Kang, Y. S. Cho, D. Jung, C. Lim, C. Lim, M.-j. Cha, S.-P. Lee, T. Hyeon, D.-H. Kim, Stretchable low-impedance nanocomposite comprised of Ag–Au core–shell nanowires and pt black for epicardial recording and stimulation. *Adv. Mater. Technol.* **5**, 1900768 (2020).
28. D. J. Lipomi, M. Vosgueritchian, B. C. K. Tee, S. L. Hellstrom, J. A. Lee, C. H. Fox, Z. Bao, Skin-like pressure and strain sensors based on transparent elastic films of carbon nanotubes. *Nat. Nanotechnol.* **6**, 788–792 (2011).
29. J. Zhang, X. Liu, W. Xu, W. Luo, M. Li, F. Chu, L. Xu, A. Cao, J. Guan, S. Tang, X. Duan, Stretchable transparent electrode arrays for simultaneous electrical and optical interrogation of neural circuits in vivo. *Nano Lett.* **18**, 2903–2911 (2018).
30. F. Xu, Y. Zhu, Highly conductive and stretchable silver nanowire conductors. *Adv. Mater.* **24**, 5117–5122 (2012).
31. S. Choi, S. I. Han, D. Jung, H. J. Hwang, C. Lim, S. Bae, O. K. Park, C. M. Tschabrunn, M. Lee, S. Y. Bae, J. W. Yu, J. H. Ryu, S. W. Lee, K. Park, P. M. Kang, W. B. Lee, R. Nezafat, T. Hyeon, D. H. Kim, Highly conductive, stretchable and biocompatible Ag-Au core-sheath nanowire composite for wearable and implantable bioelectronics. *Nat. Nanotechnol.* **13**, 1048–1056 (2018).
32. N. Matsuhisa, D. Inoue, P. Zalar, H. Jin, Y. Matsuba, A. Itoh, T. Yokota, D. Hashizume, T. Someya, Printable elastic conductors by in situ formation of silver nanoparticles from silver flakes. *Nat. Mater.* **16**, 834–840 (2017).
33. V. Martinez, F. Stauffer, M. O. Adagunodo, C. Forro, J. Vörös, A. Larmagnac, Stretchable silver nanowire–elastomer composite microelectrodes with tailored electrical properties. *ACS Appl. Mater. Interfaces* **7**, 13467–13475 (2015).
34. H. Zhao, Y. Zhou, S. Cao, Y. Wang, J. Zhang, S. Feng, J. Wang, D. Li, D. Kong, Ultrastretchable and washable conductive microtextiles by coassembly of silver nanowires and elastomeric microfibers for epidermal human–machine interfaces. *ACS Mater. Lett.* , 912, 920 (2021).
35. B. Lu, H. Yuk, S. Lin, N. Jian, K. Qu, J. Xu, X. Zhao, Pure PEDOT:PSS hydrogels. *Nat. Commun.* **10**, 1043 (2019).
36. C. Keplinger, J.-Y. Sun, C. C. Foo, P. Rothemund, G. M. Whitesides, Z. Suo, Stretchable, transparent, ionic conductors. *Science* **341**, 984–987 (2013).
37. I. D. Joshipura, H. R. Ayers, C. Majidi, M. D. Dickey, Methods to pattern liquid metals. *J. Mater. Chem. C* **3**, 3834–3841 (2015).
38. M. D. Dickey, Stretchable and soft electronics using liquid metals. *Adv. Mater.* **29**, 1606425 (2017).
39. J. Yan, Y. Lu, G. Chen, M. Yang, Z. Gu, Advances in liquid metals for biomedical applications. *Chem. Soc. Rev.* **47**, 2518–2533 (2018).
40. S. Cheng, C. Hang, L. Ding, L. Jia, L. Tang, L. Mou, J. Qi, R. Dong, W. Zheng, Y. Zhang, X. Jiang, Electronic blood vessel. *Matter* **3**, 1664–1684 (2020).
41. J.-H. Kim, S. Kim, J.-H. So, K. Kim, H.-J. Koo, Cytotoxicity of gallium–indium liquid metal in an aqueous environment. *ACS Appl. Mater. Interfaces* **10**, 17448–17454 (2018).
42. X. Li, M. Li, L. Zong, X. Wu, J. You, P. Du, C. Li, Liquid metal droplets wrapped with polysaccharide microgel as biocompatible aqueous ink for flexible conductive devices. *Adv. Funct. Mater.* **28**, 1804197 (2018).
43. Y. Cui, F. Liang, Z. Yang, S. Xu, X. Zhao, Y. Ding, Z. Lin, J. Liu, Metallic bond-enabled wetting behavior at the liquid Ga/$CuGa_2$ interfaces. *ACS Appl. Mater. Interfaces* **10**, 9203–9210 (2018).
44. H. Zhu, S. Wang, M. Zhang, T. Li, G. Hu, D. Kong, Fully solution processed liquid metal features as highly conductive and ultrastretchable conductors. *npj Flexible Electron.* **5**, 25 (2021).

45. J. Tang, X. Zhao, J. Li, R. Guo, Y. Zhou, J. Liu, Gallium-based liquid metal amalgams: Transitional-state metallic mixtures (TransM^{2}ixes) with enhanced and tunable electrical, thermal, and mechanical properties. *ACS Appl. Mater. Interfaces* **9**, 35977–35987 (2017).
46. P. Le Floch, N. Molinari, K. Nan, S. Zhang, B. Kozinsky, Z. Suo, J. Liu, Fundamental limits to the electrochemical impedance stability of dielectric elastomers in bioelectronics. *Nano Lett.* **20**, 224–233 (2020).
47. D. Ponnamma, K. K. Sadasivuni, Y. Grohens, Q. Guo, S. Thomas, Carbon nanotube based elastomer composites – An approach towards multifunctional materials. *J. Mater. Chem. C* **2**, 8446–8485 (2014).
48. W. Wang, S. Wang, R. Rastak, Y. Ochiai, S. Niu, Y. Jiang, P. K. Arunachala, Y. Zheng, J. Xu, N. Matsuhisa, X. Yan, S.-K. Kwon, M. Miyakawa, Z. Zhang, R. Ning, A. M. Foudeh, Y. Yun, C. Linder, J. B. H. Tok, Z. Bao, Strain-insensitive intrinsically stretchable transistors and circuits. *Nat. Elect.* **4**, 143–150 (2021).
49. Y. Wang, C. Zhu, R. Pfattner, H. Yan, L. Jin, S. Chen, F. Molina-Lopez, F. Lissel, J. Liu, N. I. Rabiah, Z. Chen, J. W. Chung, C. Linder, M. F. Toney, B. Murmann, Z. Bao, A highly stretchable, transparent, and conductive polymer. *Sci. Adv.* **3**, e1602076 (2017).
50. J. Y. Oh, S. Kim, H.-K. Baik, U. Jeong, Conducting polymer dough for deformable electronics. *Adv. Mater.* **28**, 4455–4461 (2016).
51. I. M. Graz, D. P. J. Cotton, S. P. Lacour, Extended cyclic uniaxial loading of stretchable gold thin-films on elastomeric substrates. *Appl. Phys. Lett.* **94**, 071902 (2009).
52. J. Qu, L. Ouyang, C.-c. Kuo, D. C. Martin, Stiffness, strength and adhesion characterization of electrochemically deposited conjugated polymer films. *Acta Biomater.* **31**, 114–121 (2016).
53. V. R. Feig, H. Tran, M. Lee, Z. Bao, Mechanically tunable conductive interpenetrating network hydrogels that mimic the elastic moduli of biological tissue. *Nat. Commun.* **9**, 2740 (2018).
54. J. Goding, A. Gilmour, P. Martens, L. Poole-Warren, R. Green, Interpenetrating conducting hydrogel materials for neural interfacing electrodes. *Adv. Healthc. Mater.* **6**, 1601177 (2017).
55. C. H. Hakansson, Conduction velocity and amplitude of the action potential as related to circumference in the isolated fibre of frog muscle. *Acta Physiol. Scand.* **37**, 14–34 (1956).
56. C. A. Herman, E. J. Sandoval, Catecholamine effects on blood pressure and heart rate in the American bullfrog, *Rana catesbeiana*. *Gen. Comp. Endocrinol.* **52**, 142–148 (1983).
57. B. Lord, A. Boswood, A. Petrie, Electrocardiography of the normal domestic pet rabbit. *Vet. Rec.* **167**, 961–965 (2010).
58. S. Ghasi, A. Mbah, N. Pu, E. Nwobodo, O. Ao, G. Onuaguluch, Interventional role of piperazine citrate in barium chloride induced ventricular arrhythmias in anaesthetized rats. *Biomed. Res.* **20**, 186–191 (2009).
59. B. Liu, S. Li, Y. Su, M. Xiong, Y. Xu, Comparative study of the protective effects of terfenadine and amiodarone on barium chloride/aconitine-induced ventricular arrhythmias in rats: A potential role of terfenadine. *Mol. Med. Rep.* **10**, 3217–3226 (2014).

Acknowledgments

Funding: This work was financially supported by National Key Research and Development Program of China (grant no. 2021YFF1000700 and 2019YFA0802800), Key Research and Development Program of Jiangsu Provincial Department of Science and Technology of China (grant no. BE2019002), and High-Level Entrepreneurial and Innovative Talents Program of Jiangsu Province. **Author contributions:** D.K. and X.N. conceived the experiments. S.W. carried out material preparations, device fabrications, and characterizations. J.Z. performed SEM characterizations. H.Z. carried out contact angle and mechanical measurements. Y.N., Y.L., and S.W. performed the in vivo animal experiments. Y.X. performed the biocompatibility tests. S.W. and S.C. analyzed the experimental data. S.W. and D.K. wrote the original manuscript. All authors contributed to the scientific planning and discussions. **Competing interests:** The authors declare that they have no competing interests. **Data and materials availability:** All data needed to evaluate the conclusions in the paper are present in the paper and/or the Supplementary Materials.

Submitted 21 July 2021
Accepted 7 February 2022
Published 30 March 2022
10.1126/sciadv.abl5511